processes

MDPI

Article

Analysis Method of Full-Scale Pore Distribution Based on MICP, CT Scanning, NMR, and Cast Thin Section Imaging—A Case Study of Paleogene Sandstone in Xihu Sag, East China Sea Basin

Jinlong Chen [1,2], Zhilong Huang [1,2,*], Genshun Yao [3], Weiwei Zhang [4], Yongshuai Pan [1,2] and Tong Qu [1,2]

[1] State Key Laboratory of Petroleum Resources and Prospecting, China University of Petroleum, Beijing 102249, China; cjl2006_2007@163.com (J.C.)
[2] College of Geosciences, China University of Petroleum, Beijing 102249, China
[3] Hangzhou Institute of Geology, China National Petroleum Corporation, Hangzhou 310023, China
[4] The Fourth Geological Company of Hubei Geological Bureau, Xianning 437014, China
* Correspondence: huangzhilong1962@163.com

Abstract: Using different experimental methods, the pore radius ranges vary greatly, and most scholars use a single experiment to study pore structure, which is rarely consistent with reality. Moreover, the numerical models used in different experiments vary and cannot be directly compared. This article uniformly revised all experimental data into a cylinder model. Quantitative analysis of the full-scale pore distribution is established by mercury withdrawal–CT data, and semi-quantitative distribution is obtained by mercury–NMR–cast thin section imaging. In this paper, we introduce the tortuosity index (τ) to convert the CT ball-and-stick model into a cylinder model, and the pore shape factor (η) of the cast is used to convert the plane model into the cylinder model; the mercury withdrawal data is applied to void the influence of narrow throat cavities, and the NMR pore radius distribution is obtained using the mercury-T_2 calibration method. Studies have shown that the thickness of bound water is 0.35~0.4 μm, so the pores with different radius ranges were controlled by different mechanisms in the NMR tests, with pores < 0.35~0.4 μm completely controlled by surface relaxation, including strong bound water and weak bound water; pores in the 0.4~4 μm reange were controlled by surface relaxation; and pores > 10 μm were completely controlled by free relaxation. The surface relaxivity rate of fine sandstone was 18~20 μm/s. The tortuosity index τ was generally 1~7; the larger the value, the more irregular the pores. The pore shape factor η was generally 0.2~0.5; the smaller the value, the more irregular the pores. Mercury withdrawal–CT scan data can quantitatively determine the pore radius distribution curve. The coefficient of the logarithm is positive considering porosity, and the constant is negative considering porosity. Permeability controls the maximum pore radius, with a max pore radius > 100 μm and a permeability > 1 mD. Mercury withdrawal–NMR–cast thin section imaging data can semi-quantitatively establish a pore radius distribution histogram. The histogram represents quasi-normal, stepped, and unimodal data. When 60 μm is the inflection point, if a large proportion of pores measure > 60 μm, good reservoir quality is indicated. If a large proportion of pores measures < 60 μm, the permeability is generally <0.5 mD.

Keywords: full-scale pore distribution; CT scan; CT cylinder model; tortuosity index; NMR; mercury withdrawal

Citation: Chen, J.; Huang, Z.; Yao, G.; Zhang, W.; Pan, Y.; Qu, T. Analysis Method of Full-Scale Pore Distribution Based on MICP, CT Scanning, NMR, and Cast Thin Section Imaging—A Case Study of Paleogene Sandstone in Xihu Sag, East China Sea Basin. *Processes* **2023**, *11*, 1869. https://doi.org/10.3390/pr11071869

Academic Editor: Fabio Carniato

Received: 16 May 2023
Revised: 8 June 2023
Accepted: 19 June 2023
Published: 21 June 2023

1. Introduction

The experimental methods for pore structure analysis primarily include cast thin section imaging, scanning electron microscopy, high-pressure mercury injection, nuclear magnetic resonance (NMR), CT scanning, etc. [1–3]. Different experimental methods have varying scales for analyzing pore size; generally, the range is 1–500 μm in the observation

of thin sections [1], 0.001–100 μm using SEM observation [3,4], 0.05–50 μm according to the high-pressure mercury intrusion method [1,5,6], 0.01–200 μm for the NMR method [5–9], and 0.1–200 μm by the CT scanning method [10,11] (Figure 1). It can be seen that microscopic observation is mainly used to analyze the larger pores. Mercury intrusion, nuclear magnetism, and CT are generally used to analyze smaller pores. Different analytical methods are affected by physical principles, experimental conditions, media, etc., revealing difficulties in the unification of pore size distributions by different experimental techniques. It is easy to neglect important pore structure information if a single experimental method is used for analysis.

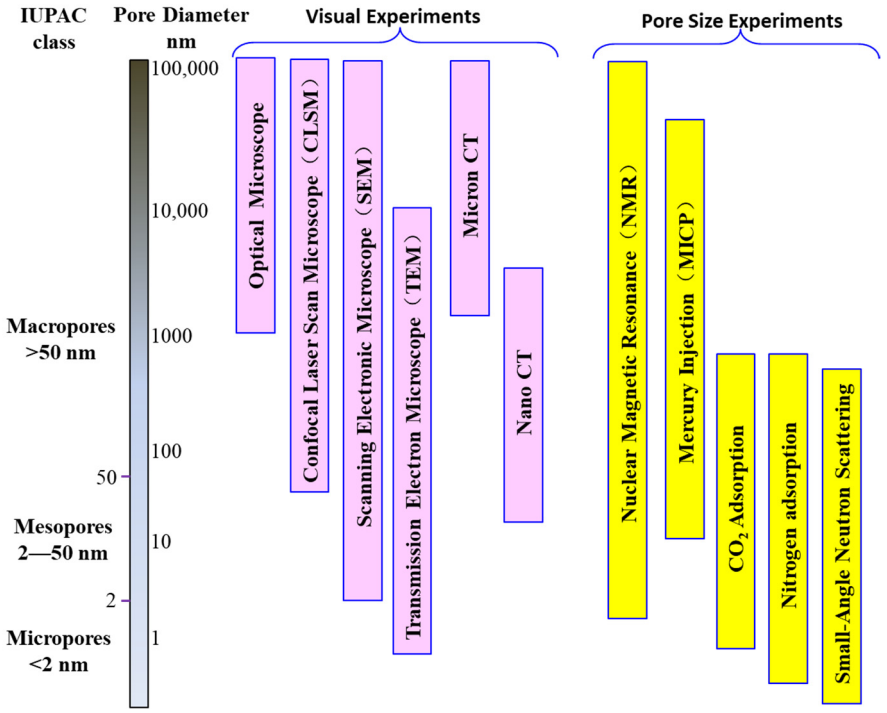

Figure 1. Pore size range of main experiments.

In this paper, a variety of experimental methods were used to analyze the Huagang Formation reservoirs in the Xihu Sag of the East China Sea Basin and to comprehensively analyze the pore information obtained by different experimental methods, thereby obtaining the characteristics of the Huagang Formation reservoir.

Microscopic observation of pore structure was conducted, and the observation of cast thin sections was conducted mainly to obtain data such as pore area, pore circumference, and equivalent pore diameter; to analyze the characteristics of primary pores, secondary dissolution pores, throats, and particle contact relationships; and to estimate the face ratio and pore size. According to the estimated pore size, the frequency histograms regarding pore size were plotted to analyze the distribution characteristics of the macropores.

High-pressure mercury intrusion mainly relies on the experimental method of gradually increasing the mercury inlet pressure corresponding to the mercury inlet volume to analyze the pore structure. It is commonly used to analyze the pore distribution characteristics of the reservoir at 0.005–10 μm. Generally, the range of 0.05–5 μm is the most accurate. The high-pressure mercury intrusion method mainly uses the clustered tube model, i.e., the pores are considered to be composed of capillary bundles with a spectrum of sizes. The mercury inlet volume represents the pore volume of all pores after passing through a certain throat [12–15], and the mercury withdrawal volume represents the volume of certain pores, but it is affected by "dead pores" [12,16].

Nuclear magnetic resonance is an experimental method used to detect water/oil content based on the magnetization of the rotating H nucleus in a stable magnetic field, as

well as the relaxation after the evacuation of the magnetic field (longitudinal relaxation T_2, transverse relaxation T_1). Without considering free relaxation and diffusion relaxation, the longitudinal relaxation time (T_2) is approximately equal to the surface relaxation [17–21]. The surface relaxation is related to the pore size. When the cylinder model is used, the pore size $r \propto T_{2surface} \approx T_2$ [18,22], and the surface relaxivity can be obtained by comparing the results of nuclear magnetic resonance and high-pressure mercury intrusion experiments. In this way, the T_2 relaxation time can be converted into pore distribution characteristics [23–25]. The pore size for detection is generally 0.001–100 μm.

CT scanning relies on the projection slices of the core when they are irradiated with X-rays. With the aid of computer analysis, the projection slices are digitally processed to obtain the 3D core distribution information. In practical use, the appropriate core size was selected, depending on the pore size range. The core plug with a diameter of 2–3 mm was selected for analysis, and its analytical pore size range was generally 0.1~200 μm [10,11]. The primary parameters used are pore–throat ratio, coordination number (connectivity parameter), and connected pore data, such as that obtained from the spatial distribution diagram.

The mathematical models of these four experimental methods are different. Cast thin section imaging uses a planar model, which is unable to quantitatively obtain 3D pore data. Mercury injection uses a tube model, but this method is greatly affected by the narrow throat cavity. NMR uses a cylinder model, but the enhanced free relaxation effect of large pores can distort the data. CT uses a ball-and-stick model, but in this method, small pores are difficult to identify.

Therefore, the primary work of this article is to revise all experimental data into a cylindrical model and then analyze the pore radius distribution using semi-quantitative and quantitative methods, evaluating the relationship between pore radius distribution and core properties.

The cast thin section images and the CT data are those requiring modification. The cast thin section data uses the pore shape factor (η) to determine the function of the pore radius and length. Then, according to the pore area, the pore radius and corresponding pore volume can be determined, so the semi-quantitative pore radius distribution histogram can be established. Introducing a tortuosity index (τ), which is obtained from the surface area and volume of the CT raw data, using τ to establish a function of the pore radius and pore length, combined with the pore volume, a quantitative distribution curve of the pore radius can be determined.

Mercury intrusion and NMR do not demand model conversion, but do require data calibration. The mercury injection data uses a cylindrical model, but this method is greatly influenced by the narrow throat cavity, so using mercury withdrawal data can better reflect the small pores. The NMR T_2 spectrum can be converted into the pore radius distribution using the surface relaxation rate, but the surface relaxation rate must be calibrated [26–28].

2. Samples and Experiments

This article uses the tight sandstone in the central tectonic zone of the Xihu Sag as a representative case to analyze the semi-quantitative and quantitative full pore size distribution, which is beneficial for the use of other scholars. However, it should be pointed out that the experimental method for shale is different from that for tight sandstone, and case studies cannot cover all situations; thus, case studies reflect boundary conditions.

2.1. Sample Information

The study area is located in the Xihu Sag of the East China Sea Basin. The East China Sea Basin is a large offshore basin located off Shanghai and north of Taiwan Island in China. The Xihu Sag is located in the central part of the East China Sea Basin. It measures about 350 km from north to south and about 150 km from east to west, covering an area of around 50,000 km^2. The Xihu Sag consists of the western slope zone, the central structural overturn zone, and the eastern fault step zone, from west to east. At present, the relatively mature

exploration areas are the central and southern parts of the central structural belt, and the central part of the western slope belt. The core samples used in this paper were recovered from a total of six wells, of which five are located in the central structural overturning zone, and one is located in the western slope belt (Figure 2).

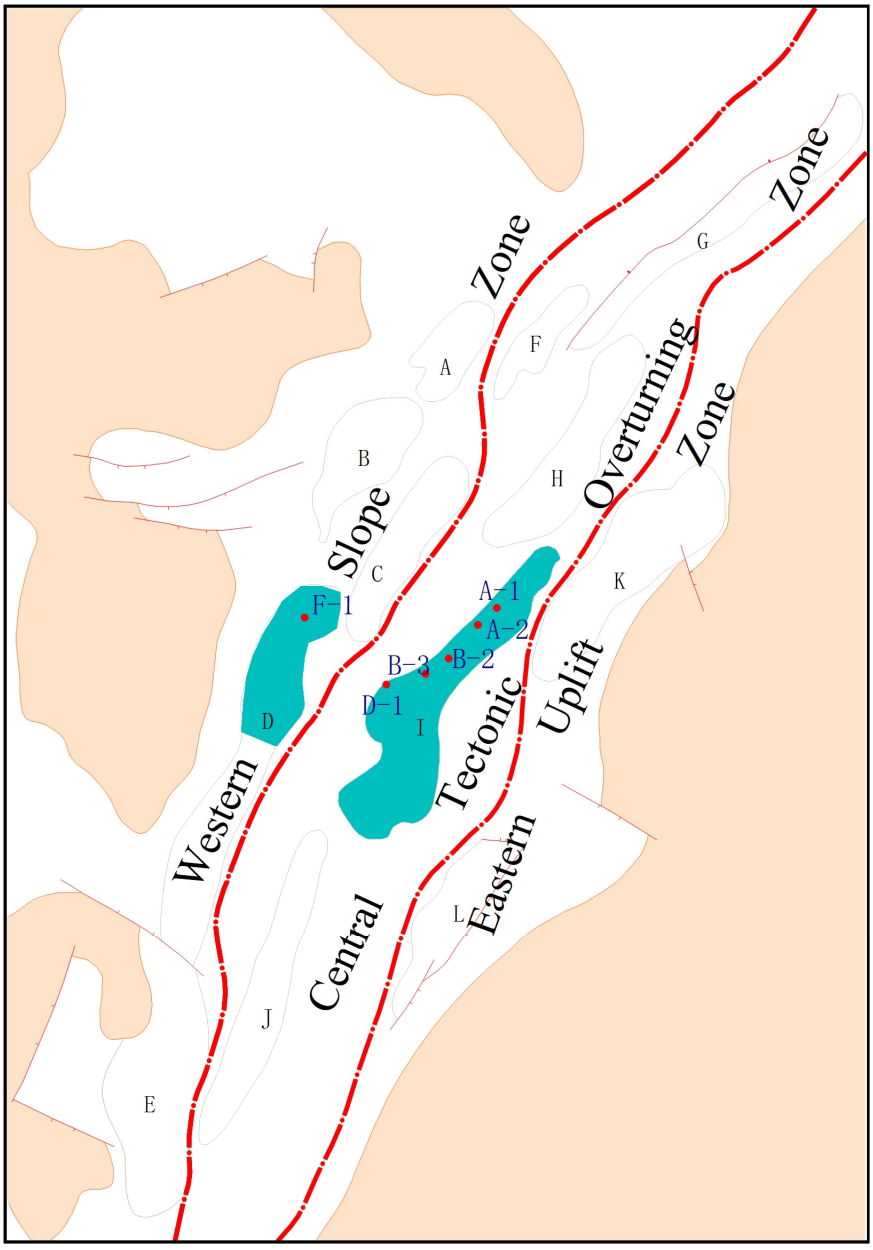

Figure 2. Structural division of Xihu Sag and location of the study area.

The stratum of the Xihu Sag is mainly the Cenozoic strata, including the Lower Eocene Baoshi Formation (E_2b), the Middle-Upper Eocene Pinghu Formation (E_2P), the Oligocene Huagang Formation (E_3h), the Lower Miocene Longjing Formation (N_1l), and the Miocene Yuquan Formation (N_1y). The primary reservoir in the western slope zone is the Pinghu Formation (E_2P), which is a bay-tidal platform deposit. The lithology primarily includes dark mudstone, coal stone, and fine sandstone, dominated by the lithological combination of mudstone intercalated with thin argillaceous siltstone and mudstone, including coal rock, thick fine sandstone, and thin coal seam. The main reservoir in the central structural overturn zone is the Huagang Formation (E_3h), which is a fluvial-lacustrine deposit. The lithology primarily includes variegated mudstone, gray mudstone, fine sandstone, and

medium-coarse sandstone. The lithological combination is mainly thick and fine sandstone, including thin mudstone, interbedded sand and mudstone, variegated mudstone, and thin muddy siltstone (Figure 3).

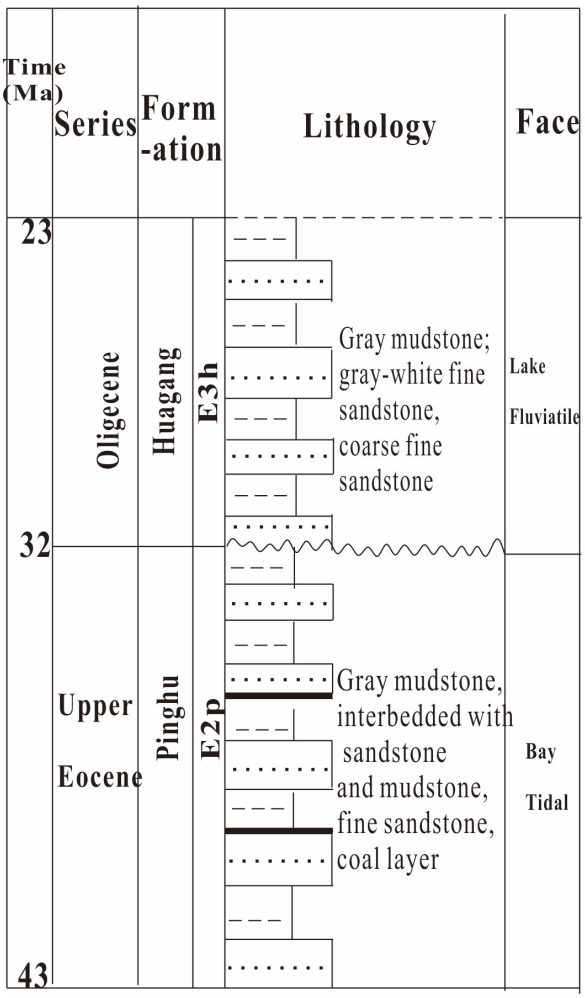

Figure 3. Layout of the structure in the Xihu Sag.

Twelve samples were selected from the Xihu Sag, including eleven cores from the Huagang Formation in the central structural belt and one core from the Pinghu Formation in the western slope belt (Table 1). The offcuts after slicing off both ends of the core plug were used to prepare cast thin sections and fresh surface samples for SEM observation. A complete core plug sample has a diameter of 2.5 cm and a length of 4–5 cm. The porosity and permeability of the core samples were measured first. The resulting sample was drilled with a micro drill bit to create a micro plunger perpendicular to the plunger axis. The diameter of the micro plunger was 2 mm, and the length was about 3–5 mm. In this paper, a total of three micro core plug were drilled, including the cores from three wells. The drilled micro core plug was subjected to CT scanning to detect its pore space distribution characteristics. After the micro core plug was drilled, two sections of the core plug were sliced and dried. After vacuum drying, all samples were saturated by pressurized water. Generally, the vacuum maintained kept for 4–6 h, the pressure for water saturation was 30 MPa, and the saturation time was 24 h. All water-saturated cores were tested using the T_2 relaxation time spectrum of saturated water nuclear magnetic resonance in order to analyze the characteristics of pore radius distribution, and 4 samples were selected for centrifugal NMR evaluation. After the nuclear magnetic resonance experiment was completed, the cores were dried. A total of 8 cores were selected from the dried core plug, and plungers with a length of 3 cm were cut. These samples were sent to the laboratory to

undergo the high-pressure mercury intrusion experiment. The maximum mercury inlet pressure of the high-pressure mercury intrusion experiment was 200 MPa (Figure 4).

Table 1. Basic information table for experimental samples.

No.	Well No.	Horizon	Practical Depth/m	Lithology	Porosity/Φ	Permeability/K	CT Scanning	Water-Saturated NMR	Centrifuged NMR	MICP	SEM	Cast Thin Section Imaging
A1	A-1	H3	3449	Siltstone	7.6	0.091	√	√	√	√	√	√
A4	A-1	H4	3823.1	Siltstone	11.2	1.946		√		√	√	√
A5	A-1	H4	3831.6	Fine sandstone	10.6	1.018		√	√		√	√
A7	A-2	H3	3614.9	Fine sandstone	10	8.152	√	√	√	√	√	√
A9	A-2	H6	4318.9	Fine sandstone	6.6	0.169		√		√	√	√
A10	A-2	H6	4320.9	Siltstone	8	0.344		√			√	√
A17	B-2	H3b	3752.7	Siltstone	10.7	2.623		√		√	√	√
A20	B-2	H4b	4008	Fine sandstone	7.5	0.291		√		√	√	√
A22	B-3	H5a	4300.7	Siltstone	7.4	0.324		√		√	√	√
A25	D-1	H3	4324.9	Fine sandstone	8.2	1.394		√			√	√
A26	D-1	H8	5106.9	Fine sandstone	8.5	0.369	√	√	√	√	√	√
A45	F-1	P10	4106.86	Medium sandstone	12.5	5.292		√			√	√

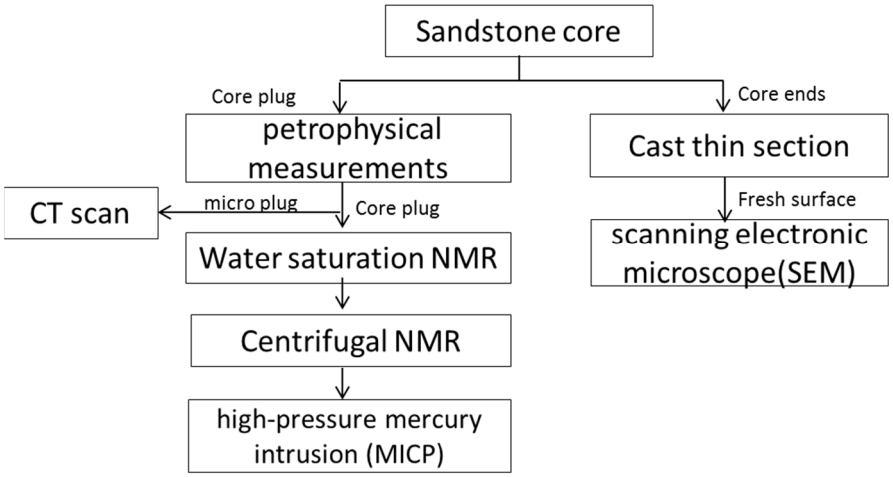

Figure 4. Flow chart for the core experiment.

2.2. Experiment

This article mainly uses four types of experiments: cast thin section imaging, CT, NMR, and mercury intrusion. Cast thin section imaging is a semi-quantitative experimental method, while CT is a quantitative experimental method. After the NMR–mercury calibration, this technique can be considered a quantitative method. Scanning electron microscopy is mainly used to determine whether the pores are suitable for use with the ball-and-stick model or the cylindrical model.

(1) Scanning electron microscopy

Scanning electron microscope observation was conducted using a Quanta 200 F field emission scanning electron microscope, which has a resolution of nanometers and a maximum magnification of 200,000 times. It can be used for energy spectrum measurement and analysis of the element content of selected areas, and it is widely used for the surface morphology and composition analysis of solid materials, including rock minerals, metal materials, polymer materials, ceramics, biological materials, nanomaterials, etc. It is necessary to use a fresh rock surface for the analysis of minerals and primary pores.

(2) Cast thin section imaging

Leica DMRXHC and Linkam THMSG600 optical microscopes were used for the observation of the cast thin sections. The magnification was 25–500 times, and blue cast rubber was generally used for sandstone, with a filling pressure of 0.8–1.3 MPa. The thickness of the polished sample was 0.04 mm. A glass cover was applied, depending on the situation.

(3) X-ray CT scanning

The basic working principle of X-ray CT scanning (CT for short) is to use rays to penetrate an object, and the intensity of X-rays passing through the object is related to the density of the object. When the amount of X-ray photons I_0 passes through any volume with a linear attenuation coefficient μ, the time quantum becomes I in the elementary time, and the process follows the Beer-Lambert Law, collects the data obtained by continuously changing the scanning angle, and then reconstructs the collected data image into a CT cross-sectional scanned image of the object, thereby forming a gray value image. The scanned two-dimensional gray image was reconstructed, and the CT data was processed by the analysis algorithm using professional image calculation and processing software to obtain the image. The CT scan used the German Bruker SkyScan2211 scanner, with an image pixel of 1024 × 1024 and a minimum resolution controlled by the sample size [10]. Its resolution reached 1~2 μm, when a 2 mm diameter micro plunger was used.

(4) High-pressure mercury injection

The high-pressure mercury intrusion was analyzed by an AutoPore III 9505 pore size analyzer. The maximum mercury inlet pressure was 200 MPa, and the corresponding pore radius was 3.7 nm. The core in the study area was selected in order to use the highest mercury inlet pressure of 100 MPa, and its pore radius was 7.3 nm, which is adequate for research requirements.

(5) Nuclear magnetic resonance experiment

The NMR experiment was conducted by using a MacroMR12–150H device, with a frequency of 12.80 MHz, a magnet strength of 0.3 T, and a coil diameter of 25 mm. During the experiment, the echo interval was set to 0.15 ms, and the time for measurement was 8000 ms. By using the CPMG sequence [26], the relaxation time range after inversion was 0.001~10,000 ms. The NMR experiment was conducted using water saturation and centrifugal treatments. The saturation of the core by water was conducted using the vacuum pressure saturation method. The centrifugal velocity was generally 1500 rpm, 3000 rpm, 4000 rpm, etc., with maximum centrifugal velocity of 7000 rpm.

3. Results and Discussion of the Semi-Quantitative Methods

Semi-quantitative experiments mainly include cast thin section imaging and NMR. In order to convert the NMR T_2 spectrum into the pore radius distribution, this section also includes the quantitative mercury intrusion experiment [1–6]. SEM is used to determine which numerical model is more suitable for pore evaluation.

3.1. Numerical Model Selection Based on SEM

From the observation of pore space by SEM, the distribution of void space occurred mostly in the form of cells, channels, bundles, and irregularities [29].

According to SEM observations, larger pores are suitable for both ball and cylinder models (Figure 5a). If the pore size is small, it is suitable for cylindrical models (Figure 5b), especially for pores of a few micrometers (Figure 5c). Even if the pores are very irregular, the cylindrical model can still describe them well. Therefore, this article uses a cylindrical model, which can obtain more reliable data, for analysis.

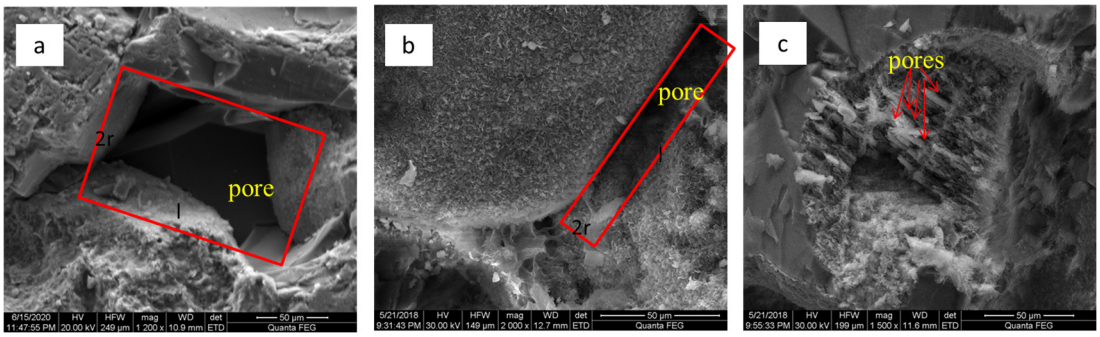

Figure 5. Distribution characteristics of pore space. (**a**) Well D-1 is 4324.9 m, with cellular pores, and the pore volume is approximately equal to the volume of the red frame rock rotated 360° on the long axis; (**b**) Well A-2 is 3614.9 m, with channel-like, mainly primary residual pores, and cementation of clay minerals; (**c**) Well A-1 is 3831.6 m, with bundle-like pores formed by feldspar dissolution, with a pore radius generally <5 μm (Arrows pointing towards pores).

3.2. Results and Recalculation of Cast Thin Section Data

In this paper, generally, the parameters such as pore radius and pore volume were used. In the observation of cast thin section imaging, the pores represented varying morphologies, including oval, rectangular, moon-shaped, and nearly triangular shapes. The radius of the short axis of the pore was generally 10–60 μm, and that of individual primary residual pores was more than 100 μm.

For the total pore volume, 3–5 viewing areas were generally used, and the data were integrated under all viewing areas.

If semi-quantitative analysis is conducted using cast thin section data, there should be several key assumptions: ① the maximum cross-sectional area of the pores observed in the cast thin section should be used, ② the planar features should represent the spatial features, and ③ image processing software should effectively identify the pores. These assumptions are achievable for sandstone, but difficult to achieve for shale; thus, when studying shale using this method, one should be more cautious.

For the total pore volume, 3~5 viewing areas were generally used, and the data were integrated under all viewing areas. The pore area and pore perimeter data were selected, and the pore shape factor was calculated by the following formula:

$$\eta = \frac{4\pi A}{L^2} \tag{1}$$

Among these, η is the pore shape factor, no units; A is the pore area, μm^2; and L is the pore perimeter, μm.

The pore radius is determined by the following formula:

$$r = \frac{\eta L}{\sqrt{8\pi}} = \sqrt{2\pi} \times \frac{A}{L} \tag{2}$$

The pore volume is calculated by the following formula:

$$V = \frac{\pi r^3}{\eta} = \frac{\left(\sqrt{2\pi}\right)^3}{4} \times \frac{A^2}{L} \tag{3}$$

Among them, r is pore radius, μm; V is pore volume, μm^3.

It should be pointed out that the above methods require raw data exported by image processing software. If there are many viewing areas and a large amount of data, establishing a pore radius distribution curve (which is also semi-quantitative data) should be

considered. This article only covers 3~5 viewing areas, and the amount of data is not sufficient to establish curves. Only histograms can be generated.

When the pore radius was less than 100 μm, the statistics were represented by segmentation according to 10 μm, and the pores larger than 100 μm were divided into 100~200 μm and >200 μm. By using this method, 12 cast thin samples were evaluated in the study area (Table 2), of which 8 samples corresponded to those used in the high-pressure mercury intrusion experiment.

Table 2. Estimation of pore volume frequency of different samples.

Pore Radius μm	A1 Volume %	A4 Volume %	A5 Volume %	A7 Volume %	A9 Volume %	A10 Volume %	A17 Volume %	A20 Volume %	A22 Volume %	A25 Volume %	A26 Volume %	A45 Volume %
0~10	19	9	13	5	24	13	9	13	19	15	23	5
10~20	21	15	24	4	34	24	12	26	35	18	41	8
20~30	27	22	16	10	21	20	10	14	17	16	17	12
30~40	11	17	21	13	9	18	21	26	13	16	11	15
40~50	8	12	9	13	5	15	8	15	11	10	8	11
50~60	14	20	13	15		10	12	6	5	11		14
60~70				10			7			9		7
70~80				9	7		4			5		6
80~90				5			6					8
90~100				7			11					9
100~200		5	4	9								5
>200												

Pore volume analysis based on the observation of the cast thin sections can roughly divide the pore radius distribution into three types. The first type was dominated by small pores, represented by six core samples with a permeability less than <0.5 mD, including A1 (Well A-1, 3449 m), A9 (Well A-2, 4318.9 m), A10 (Well A-2, 4320.9 m), A20 (Well B-2, 4008 m), A22 (Well B3, 4300.7 m), A26 (Well D-1, 5106.9 m), and A25 (Well D-1, 4324.9 m), with a permeability of 1.3 mD (Figure 6a,b). The second type was dominated by small pores with a few large pores, represented by samples such as A4 (Well A-1, 3823.1 m) and A5 (Well A-1, 3831.6 m), with a permeability of 1~2 mD (Figure 6c). The third type was characterized by the existence of a large number of miscellaneous types of pores. The representative samples were A7 (Well A-2, 3614.9 m) and A45 (Well F-1, 4106.86 m), with a permeability > 5 mD, and A17 (Well B-2, 3752.7 m), with a permeability of 2.6 mD (Figure 6d).

3.3. Results and Discussion of NMR

3.3.1. Result of Water Saturated NMR T_2 Spectrum

The water-saturated NMR experiment was conducted in 12 samples, with a length of 3~4 cm. After water saturation by vacuuming and pressuring, the water-immersed porosity was measured according to the weight changes before and after saturation (Table 3). After calculation, the water-immersed porosity of the core samples was 5%~10%, which was slightly lower than the porosity measured by air, with a factor of 0.5%~1.5%.

The NMR T_2 spectrum of samples saturated with water was mainly used to analyze the signal intensity corresponding to different T_2 relaxation times. The signal intensity represented the size of the water volume. The greater the signal intensity, the larger the water volume. According to the T_2 spectrum, the 12 cores can be simply divided into three types. The first type of reservoir was dominated by a short relaxation time, with a T_2 relaxation time range of 0.02~800 ms. The short relaxation time of 0.02~5 ms accounted for a relatively high proportion, primarily including the samples A1 (Well A-1, 3449 m), A9 (Well A-2, 4318.9 m), A10 (Well A-2, 4320.9 m), A20 (Well B-2, 4008 m), A22 (Well B3, 4300.7 m), and A26 (Well D-1, 5106.9 m), with permeability values of 0.1~0.5 mD and porosity values of 6%~8% (Figure 7a,b).

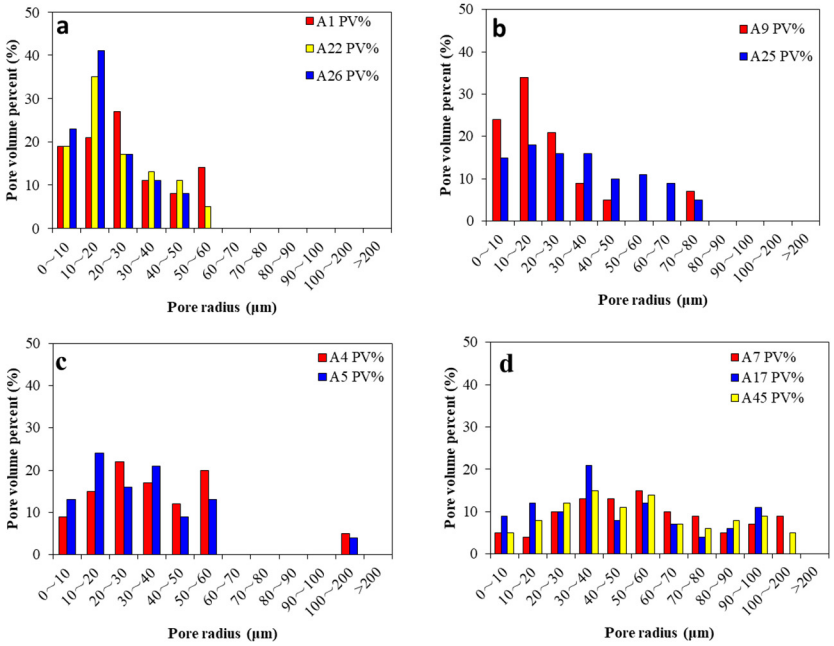

Figure 6. Pore radius distribution diagram based on observation of cast thin sections. (**a**) Samples dominated by pores smaller than 60 μm; (**b**) samples dominated by pores smaller than 80 μm; (**c**) samples dominated by pores smaller than 60 μm and the development of pores larger than 100 μm; (**d**) samples with the large distribution of miscellaneous pore sizes.

Table 3. Basic data for core saturated water.

No.	Lithology	Measured/Φ	Measured/K	Length/cm	Diameter/cm	Dry Weight/g	Water Saturated/g	Water Imbibed/g	Water Immersion Porosity/Φ
A1	Siltstone	7.6	0.091	3.71	2.47	44.8377	45.8624	1.0247	5.8
A4	Siltstone, fine sandstone	11.2	1.946	4.07	2.47	45.999	47.8797	1.8807	9.6
A5	Fine sandstone	10.6	1.018	3.64	2.47	41.599	43.2309	1.6319	9.4
A7	Fine sandstone	10	8.152	3.53	2.47	40.6202	42.1702	1.55	9.2
A9	Fine sandstone	6.6	0.169	4.11	2.48	49.1435	50.295	1.1515	5.8
A10	Siltstone, fine sandstone	8	0.344	3.36	2.48	40.0286	41.0928	1.0642	6.6
A17	Siltstone, fine sandstone	10.7	2.623	4.03	2.51	47.047	49.0348	1.9878	10
A20	Fine sandstone	7.5	0.291	4.07	2.47	47.9825	49.1404	1.1579	5.9
A22	Siltstone, fine sandstone	7.4	0.324	4.15	2.48	48.8936	50.1391	1.2455	6.2
A25	Fine sandstone	8.2	1.394	3.47	2.49	41.5419	42.7109	1.169	6.9
A26	Fine sandstone	8.5	0.369	3.39	2.47	39.6837	40.8165	1.1328	7
A45	Medium sandstone	12.5	5.292	3.05	2.49	34.982	36.5207	1.5387	10.4

The short relaxation time and long relaxation time of the second type of reservoirs were similar. The T_2 relaxation time was generally 0.03~2000 ms, with a short relaxation time of 0.03~5 ms and a long relaxation time of 5~200 ms, exhibiting basically the same proportions. The representative samples were A4 (Well A-1, 3823.1 m), A5 (Well A-1, 3831.6 m), A17 (Well B-2, 3752.7 m), and A25 (Well D-1, 4324.9 m), with permeability values of 1~3 mD and porosity values of 8%~11% (Figure 7c). The third type of reservoir was dominated by a long relaxation time, with a long relaxation time of 5~500 ms accounting

for a relatively high proportion. The representative samples were A7 (Well A-2, 3614.9 m) and A45 (Well F-1, 4106.86 m), with permeability values of 5~8 mD and porosity values of 10%~13% (Figure 7d).

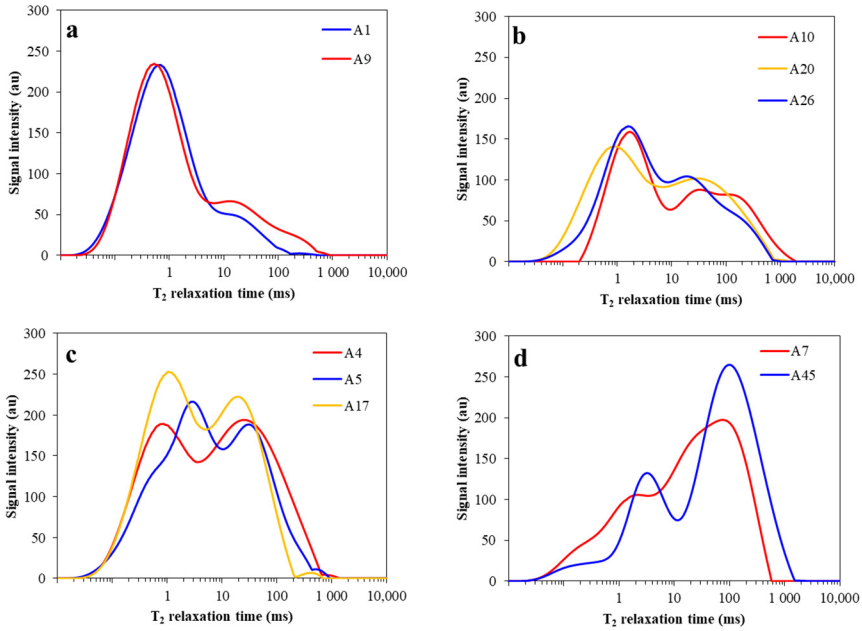

Figure 7. Characteristics of the NMR T_2 spectrum of water-saturated samples. (**a**) Samples dominated by a short relaxation time; (**b**) samples dominated by a short relaxation time, but possessing some with a long relaxation time; (**c**) samples with similar long and short relaxation times; (**d**) samples dominated by a long relaxation time.

3.3.2. Discussion of Bound Water Thickness Based on Centrifugation-NMR

Four samples of A1, A5, A7, and A26 were selected for centrifugal NMR experiments. Among them, the water content of sample A1 was low, and the curve was abnormal; therefore it was discarded during the process. For samples A5 and A7, there appeared a phenomenon that the water-saturated NMR curve could not be overlapped with the low relaxation time interval at 1500 rpm. This is mainly due to the evaporation of water on the rock surface, which causes the relaxation time of the water film on the rock surface to be recorded. The occurrence of this phenomenon has no effect on the analysis of the experimental data.

For sample A26, the NMR curve interval, with a relaxation time less than 10 ms, overlapped under the condition of water saturation, at 1500 rpm, and 3000 rpm centrifugation. Samples, such as A5 and A7, were partially overlapped in the NMR curves of less than <10 ms, indicating that 3000 rpm centrifugation cannot cause the <10 ms change in relaxation time. As the centrifugal ratio increased, the water with a relaxation time of less than 10 ms was gradually expelled out of the core by centrifugal force (Figure 8). The curves of the A5 and A26 samples, with a relaxation time of less than 1 ms, did not change at any rate, reflecting that the fluid corresponding to a relaxation time of <1 ms basically show no changes (Figure 8).

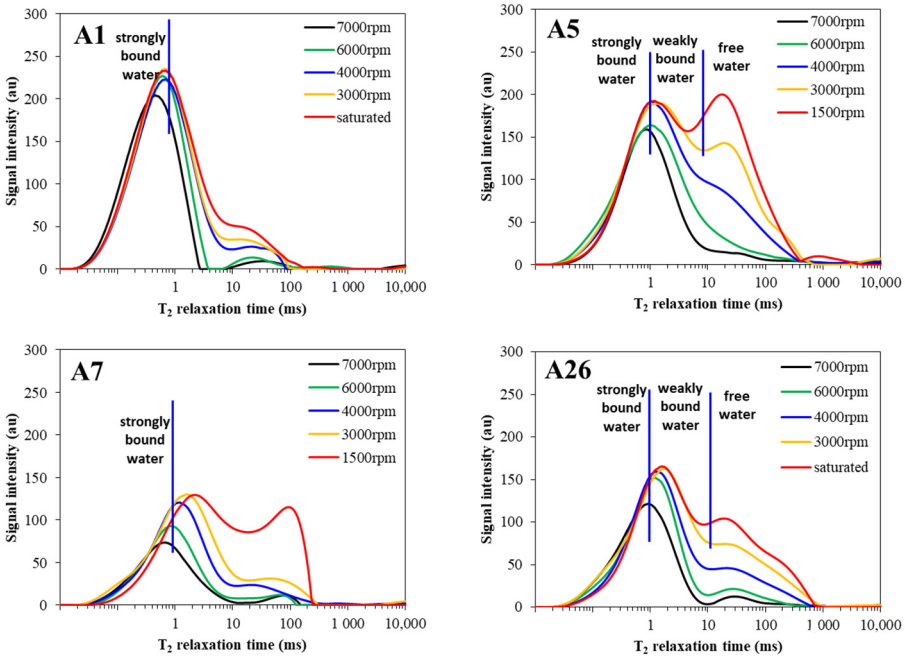

Figure 8. Characteristics of centrifugation—NMR T_2 spectrum.

NMR T_2 relaxation time is mainly composed of three periods: surface relaxation, free relaxation, and diffusion relaxation. Surface relaxation is affected by the interaction of the two-phase interface, and free relaxation is mainly controlled by single-phase fluid; diffusion relaxation can be ignored at room temperature and a lower magnetic field strength [17,18].

$$\frac{1}{T_2} = \frac{1}{T_{2free}} + \frac{1}{T_{2surface}} + \frac{1}{T_{2diffusion}} \quad (4)$$

In the formula, T_2: transverse relaxation time of pore fluid collected by the CPMG sequence; T_{2free}: transverse relaxation time of the pore fluid in a sufficiently large container; $T_{2surface}$: transverse relaxation time caused by surface relaxation; $T_{2diffusion}$: transverse relaxation time of the pore fluid caused by diffusion under the magnetic field gradient.

The water at the surface of the mineral walls was divided into three layers, namely movable water, weakly bound water, and strongly bound water [30,31]; the pore walls are the same. When the pores are large, there are three states of water. When the pores are small, there are only two states: weakly bound water and strongly bound water. The state can also occur in which there is the sole occurrence of strongly bound water.

Strongly bound water and weakly bound water are greatly affected by the pore wall, and their relaxation time is mainly controlled by surface relaxation, resulting in a short relaxation time response. Free water is controlled by free relaxation, resulting in a long relaxation time response. The free water can be expelled out of the core under any centrifugal force condition, and the bound water changes only when the centrifugal force is greater than a certain threshold. Correspondingly, in the T_2 relaxation time spectrum, the point at which the shorter relaxation time begins to change is the beginning of the bound water change.

When the centrifugal rate was less than 3000 rpm, there was no change in the spectrum of T_2 time at less than 10 ms, indicating that the portion gradually expelled out of the core below 3000 rpm was free water. The portion of that water that does not change is strongly/weakly bound water. In other words, only strongly/weakly bound water is present with the maximum thickness in a pore, under the condition of 3000 rpm centrifugal force, the pore water will not change.

There is also no change in the NMR relaxation time spectrum at <10 ms; therefore, it is inferred that the relaxation time of weakly bound water at the center of this pore is

about 10 ms. According to the centrifugal force generated by 3000 rpm and the relationship between capillary pressure and pore radius, the pore radius was correspondingly calculated. The relaxation time of the water inside the pore was 10 ms.

According to the centrifugal rate, the centrifuge arm length, and the length of the core, the centrifugal rate can be converted into the bottom pressure of the core.

$$P_c = 1.097 \times 10^{-9} \Delta\rho L(R_e - \frac{L}{2})n^2 \quad (5)$$

In this formula, P_c is the centrifugal displacement pressure, MPa; $\Delta\rho$ is the density difference between the two fluids, g/cm^3; L is the core length, cm; Re is the external rotation radius of the core, cm; and n is the centrifugal rate, rpm.

The core length was 3.4~3.7 cm, with an average of 3.5 cm; the centrifugation is equivalent to the process of water driven by air; the density difference was 1 g/cm^3, and the centrifuge radius was 13.45 cm. It can be calculated that the centrifugal force was 0.4 MPa when the rate was 3000 rpm; that is, the capillary force of the core was 0.4 MPa at this time.

When the gas and water in the capillary are in equilibrium, Formula (3) can still be used:

$$P_c = \frac{2\sigma cos\theta}{r} \quad (6)$$

where, P_c is the capillary pressure, MPa; r is the radius of capillary, μm; σ is the surface tension of the existence of two phases of air and water; and the influence of air is small.

The experimental condition is set at room temperature, 20 °C; therefore, σ = 0.072 N/m; θ is the contact wetting angle; and the mineral contact angle is greatly affected by the degree of salinity, temperature, and surface active substances [32–34]; sandstone is a hydrophilic medium, the contact angle of quartz and water is about 30 °C [32], and the contact angle of clay minerals with water is 10~30° [35]. For convenience, the contact angle is 15° under the condition of air–water centrifugation. It is calculated that the pore radius corresponding to a 0.4 MPa capillary force is 0.35 μm.

When the centrifugal rate was 3000 rpm, the centrifugal force was 0.4 MPa, the capillary pressure at equilibrium was 0.4 MPa, and the corresponding pore radius was 0.35 μm. Similarly, the thickness of the strong irreducible water of the fine sandstone was nearly 0.04 μm.

Zhao [30] has shown that, when the average pore radius is greater than 0.151 μm, the degree of water saturation has a little effect on the breakthrough pressure. If the most probable pore radius of the core sample reaches 1.760 μm, the breakthrough pressure will not be impacted by the increasing water saturation. Because free water has no effect on breakthrough pressure, we can speculate that the thickness of the bound water film is between 0.15 and 1.7 μm. The calculation of the bound water film thickness of 0.35 using centrifugal force, as employed in this article, is also quite reliable.

Under short echo interval conditions, the sole occurrence of water in the pore, and the dominance of smaller pores, the free relaxation time is extremely small and can be ignored. The horizontal relaxation (T_2 relaxation) time is mainly controlled by the surface relaxation, i.e., T_2 is directly proportional to $T_{2surface}$, assuming that the pore is a cylinder with a radius of r:

$$\frac{1}{T_2} \approx \frac{1}{T_{2surface}} = \rho_2(\frac{S}{V})_{pore} = \frac{2\rho_2}{r} \quad (7)$$

where, ρ_2 is the surface relaxivity of T_2, μm/s; $(\frac{S}{V})_{pore}$ is the specific surface area of the pore, μm^{-1}; r is the pore radius, μm; and T_2 is the horizontal relaxation time, s.

From the abovementioned analysis, the relaxation time spectrum < 10 ms did not change under the condition of a small centrifugal force. However, the short relaxation time is mainly the response of surface relaxation, indicating that the thickness of the water film controlled by surface relaxation is not affected by a small centrifugal force. That is, the pore radius of 0.35 μm is the largest area dominated by surface relaxation. If the pore size is

larger, the surface relaxation will gradually decrease, and the free relaxation will gradually increase. When the relaxation time was 10 ms, the pore radius was 0.35 μm, and the surface relaxation rate ρ_2 = 18 μm/s could be obtained by incorporating Formula (7).

3.4. Results and Recalculation of Mercury Intrusion Experiments

The maximum mercury inlet pressure in the high-pressure mercury injection experiment was 100 MPa, and the pore radius was correspondingly 0.007 μm. Due to the disconnection between the pores and the original residual pores, surrounded by the peripheral small pores, the mercury inlet saturation was mainly used to reflect the total pore volume after passing through a certain throat. However, it is difficult to reflect the pore radius distribution of the actual core [12,13]. Mercury removal is a process in which the capillary pressure of a rock displaces the mercury out of the core. At this time, the mercury inside the core is a single-phase fluid. The small bellows surrounding the large pores allow mercury to flow freely, without additional pressure. The mercury withdrawal pressure and capillary pressure was at equilibrium, and the exiting mercury volume was the pore volume corresponding to radius, but it is also affected by dead pores [36–38]. In this paper, mercury withdrawal data was used to study the distribution of the pore radius (Table 4).

Table 4. Data table showing core mercury withdrawal saturation.

Mercury Withdrawal	r μm	A1 %	A4 %	A7 %	A9 %	A17 %	A20 %	A22 %	A26 %
0.13	5.33	43.3	61.4	56.4	51.7	71.7	55.4	47.5	51.2
0.19	3.82	43.5	62.9	57.8	52.1	72.8	56.0	48.0	52.1
0.32	2.26	43.8	65.2	59.9	53.0	74.6	57.5	49.4	53.9
0.47	1.56	44.7	67.2	61.4	54.6	76.1	59.0	51.1	55.5
0.68	1.08	46.7	69.6	63.0	56.8	78.0	60.9	53.2	57.4
1	0.716	49.4	72.1	64.9	59.8	80.6	63.0	55.8	59.7
1.3	0.539	51.2	73.9	66.1	62.0	81.7	64.5	57.5	61.5
2.1	0.357	53.5	76.1	67.8	65.0	83.9	66.5	59.9	64.2
2.7	0.268	54.9	77.6	68.9	67.2	85.4	68.0	61.5	66.1
4.1	0.178	56.7	79.5	70.3	70.1	87.4	70.0	63.7	68.8
5.5	0.133	58.1	80.7	71.4	72.4	88.7	71.4	65.3	70.6
7	0.106	59.1	81.6	72.2	74.1	89.7	72.5	66.5	72.0
10	0.0712	61.3	83.3	73.8	77.7	91.3	74.4	68.8	74.3
13	0.0533	62.9	84.3	74.7	79.7	92.4	75.8	70.3	75.7
17	0.0427	64.3	85.0	75.3	81.2	93.1	76.9	71.3	76.7
20	0.0356	65.6	85.7	75.9	82.7	94.0	78.2	72.7	77.8
25	0.0305	66.6	86.2	76.6	84.0	94.5	79.0	73.5	78.4
30	0.0237	67.8	86.9	77.4	85.8	95.2	80.4	74.5	79.2
40	0.0178	69.1	87.4	78.1	87.3	95.8	81.4	75.5	79.9
50	0.0142	69.8	87.8	78.4	88.2	96.2	82.2	76.2	80.3
60	0.0118	70.4	87.9	78.7	88.8	96.4	82.7	76.6	80.5
70	0.0106	70.6	88.0	78.8	89.0	96.5	82.9	76.7	80.6
85	0.00853	71.0	88.0	78.9	89.5	96.6	83.1	76.9	80.7
100	0.00725	71.2	88.0	79.1	89.7	96.7	83.2	77.1	80.7

To calculate the mercury withdrawal saturation of each pore radius interval of mercury withdrawal data, the mercury withdrawal saturation represented the pore volume percentage of this pore interval. In order to match the high-pressure mercury intrusion data with the absence of NMR data, the minimum pore radius was 0.00725 μm. By using a geometric step length to divide the interval of 0.00725~5.33 μm, the geometric magnification was 1.0719, which was the same as that of the NMR data. When a certain pressure of geometric sequence was the same as the mercury withdrawal pressure, the pore volume percentage corresponding to the mercury withdrawal pressure was recorded as the pore volume percentage of the corresponding pressure in the geometric sequence. The pore volume percentage was evenly distributed in the equal ratio, according to the algebraic

average method. At the step point in the ratio sequence, a geometric series model of the pore radius distribution of the rock can be obtained (Figure 9).

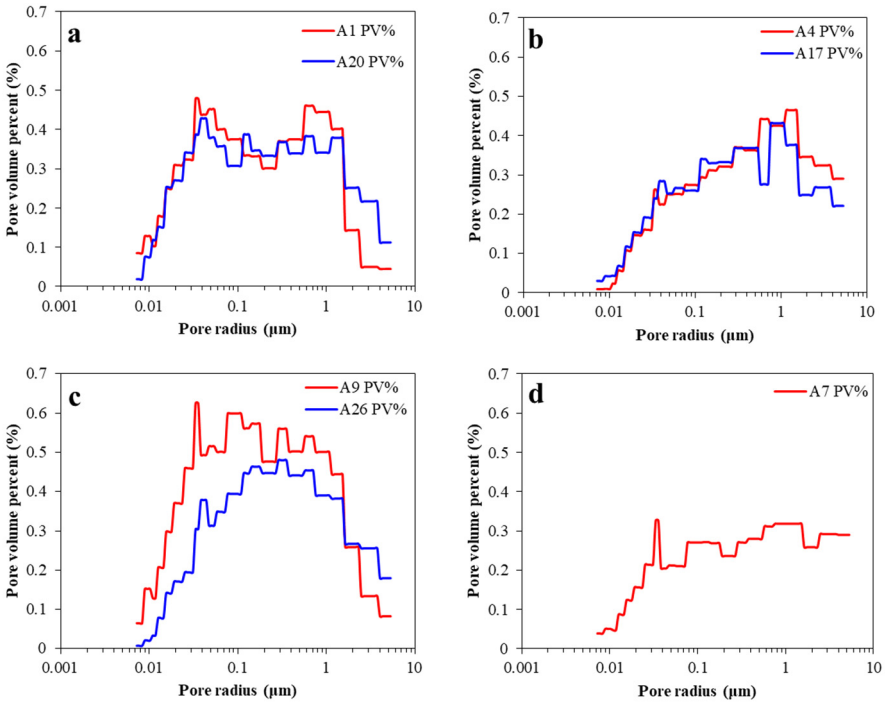

Figure 9. Distribution of mercury withdrawal pore volume percentage after conversion of equal step length. (**a**) Pore radius distribution diagram of the low-porosity and low-permeability core, with bimodal type; (**b**) pore radius distribution diagram of the unimodal type, with medium porosity and permeability; (**c**) pore radius distribution diagram of the arch type, with low permeability; (**d**) pore radius distribution diagram of the climb type, with high permeability.

According to the pore radius distribution obtained by mercury withdrawal saturation, the results can be roughly divided into four types: the bimodal type, the unimodal type, the arch type, and the climb type.

The bimodal type, with low porosity and permeability, is represented by samples including A1 (Well A-1, 3449 m), A20 (Well B-2, 4008 m), and A22 (Well B3, 4300.7 m), with permeability values of 0.1~0.3 mD and porosity values of 7%~8% (Figure 9a). Two main peaks correspond to the pore radii of 0.03 μm and 0.6 μm, generally with a smaller pore radii.

The unimodal type, with medium porosity and permeability, is represented by samples such as A4 (Well A-1, 3823.1 m) and A17 (Well B-2, 3752.7 m), with permeability values of 1~3 mD and porosity values of 10%~11% (Figure 9b). The peak was at 1 μm, and the proportion of pores with other radii was relatively low.

The arch type, with low porosity and permeability, is represented by samples A9 (A-2 Well 4318.9 m) and A26 (Well D-1, 5106.9 m), with permeability values of 0.1~0.5 mD and porosity values of 6%~8% (Figure 9c). There is no obvious peak in this type, and the proportion was relatively average, between 0.03 and 1 μm.

The climb type exhibited ascending high-permeability cores, such as those noted in sample A7 (Well A-2, 3614.9 m), with a permeability of 8 mD and a porosity of 10% (Figure 9d). There was no obvious peak in this shape, but large numbers of pores greater than 1 μm existed, and the curve showed a gradual upward pattern.

3.5. Calibration of MICP and NMR

The high-pressure mercury injection experiment includes the mercury inlet curve and the mercury withdrawal curve. The mercury inlet curve was mainly used to analyze the pore volume after passing through a certain throat. The mercury withdrawal curve was

mainly used to analyze the pore radius distribution. The analysis conducted in this paper was mainly performed by using the mercury withdrawal curve.

From the pore radius distribution transformed by the mercury withdrawal curve, it can be seen that the low porosity (<1 mD) was mainly bimodal and of the arch type (Figure 9a,c), and the medium porosity and permeability (1~5 mD) were mainly unimodal (Figure 8). The high-porosity and high-permeability samples (>5 mD) were mainly the ascending type (Figure 9d).

Unlike the water-saturated NMR curve, the water-saturated NMR curve with a low-permeability core was mainly the left-peak dominant type (Figure 7a,b), the medium-permeability core had a left-right equal peak type (Figure 7c), and the high-permeability core was of the right-peak dominant type (Figure 7d).

This is mainly due to the fact that the low NMR relaxation time contains the signal of bound water near the macropore wall. That is to say, regardless of pore size, the short relaxation time of strongly bound water will be displayed in the spectrum.

Therefore, to calibrate the mercury intrusion–NMR curve morphology, it is necessary to determine different points of fit. The bimodal type and unimodal type of mercury withdrawal curves, usually used to calibrate NMR curves. The arch type and the climb type are difficult to use for mercury intrusion-NMR comparison.

The lowest point in the middle of two peaks of the bimodal type of mercury withdrawal curve of pore radius distribution is commensurate with the middle inflection of the two peaks of the left-peak dominant NMR curve. The apex of the unimodal type of mercury pore size distribution curve is commensurate with the right peak of the NMR curve.

The NMR pore radius conversion, based on mercury withdrawal data, used the data of Samples A1, A17, and A20. For Sample A1, the low point between the two peaks of the mercury withdrawal pore radius distribution was used as the calibration point to migrate the NMR curve (Figure 10a). For Samples A17 and A20, the right peak apex was used as the calibration point to migrate the NMR curve (Figure 10b,c). It can be seen that the parameter for the conversion of NMR T_2 to pore size distribution, for the same lithology in a region, was almost constant. In the study area, the NMR T_2 can be converted into a pore size distribution curve by dividing the abscissa of the T_2 curve by 25 (Figure 10).

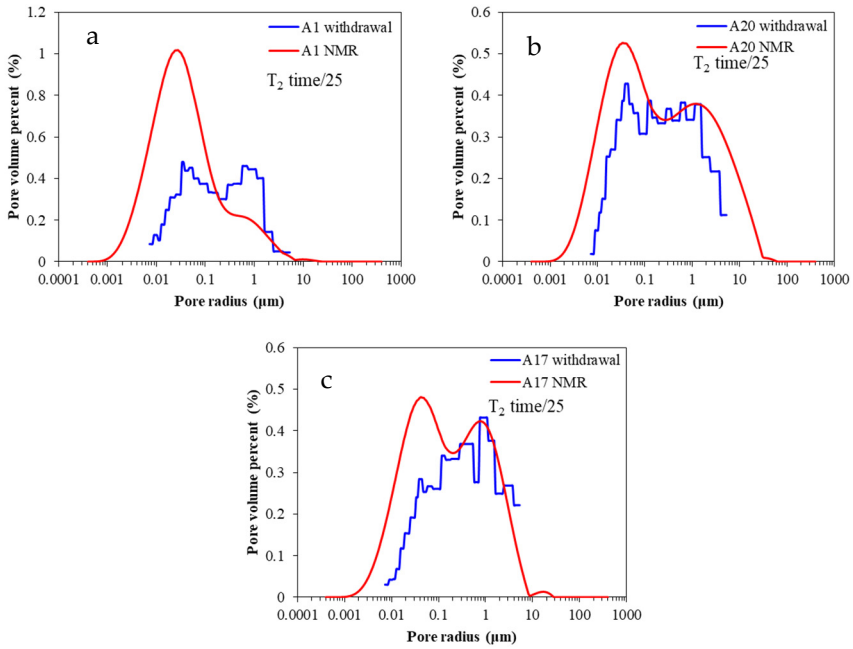

Figure 10. NMR pore radius conversion based on mercury withdrawal data.

According to the calculation of Formula (7), the surface relaxation rate of fine sandstone in the study area was ρ_2 = 20 μm/s, which was close to the surface relaxation rate

(ρ_2 = 18 μm/s) analyzed by the NMR curve after 3000 rpm centrifugation. This proved that both of the two methods are reliable.

Generally speaking, the NMR curves of fine sandstone < 10 ms (<0.4 μm) and >250 ms (>10 μm) are not recommended for pore structure analysis. The surface relaxation of the NMR curve of 10~100 ms (0.4~4 μm) accounted for a larger proportion, and the free relaxation of the NMR curve of 100~250 ms (4~10 μm) accounted for a larger proportion, but the pore analysis with limited conditions can still be carried out.

3.6. Semi-Quantitative Method for Full-Scale Pore Radius

Semi-quantitative methods mainly include cast thin section imaging, NMR, and mercury intrusion. Because of the small amount of cast section data, only a histogram can be made, so the semi-quantitative method in this paper continues to use the histogram mode. It should be pointed out that if the casting section data is sufficient, a semi-quantitative pore radius distribution curve can be established.

It is only necessary to convert the NMR spectrogram into a histogram. The mercury withdrawal pore radius range was 0.007~5.3 μm, and the nuclear magnetic pore radius range used was 0.2~10 μm. The pore radius range from the observation of the cast thin sections was <200 μm, and the three types of experimental data can be used to analyze the full-scale pore radius of the rock.

After the NMR T_2 relaxation time was converted into the pore radius by Formula (7), the NMR signal intensity was then converted into the pore volume percentage. After the aforementioned analysis, the NMR pore size curve of <0.4 μm was affected by strongly and weakly bound water, and it is difficult to accurately express the pore information, as pores of a few micrometers are considered to be greatly affected by bound water. In order to prevent the NMR pore size curve from being affected by the additional signal generated by the bound water of the large pores, the full pore size analysis does not use pore size curves below a few microns. In this paper, the NMR pore size data of 5~10 μm was mainly used, due to the fact that the NMR data of 5~10 μm was affected by free relaxation, causing difficulties in representing the pore radius information. However, the relative size of the pore radius can also be represented.

In the statistical data of the cast thin sections, the data <10 μm was affected by the driving pressure of the cast rubber (usually about 0.6~1 MPa). Some small pores may not be filled by the cast rubber, and thus cannot be accurately counted. Therefore, the statistical data of the cast thin sections < 10 μm were not used; only the >10 μm portions was employed.

Both high-pressure mercury intrusion and nuclear magnetism are methods that use volumetric measurement. After the cast thin section was converted into a cylinder, it remained as volume data. Therefore, the weights of these three types of experiments were all normalized to be 1, and no additional processing was required. Only the mercury withdrawal of <5 μm, the NMR pore volume data of 5~10 μm, and the statistical data of cast thin section of >10 μm were spliced together, and then the pore volume data was calibrated to 100% to obtain the characteristics of the full-scale pore size distribution (Figure 11).

The semi-quantitative full-scale pore radius distribution was mainly divided into three types of distribution characteristics, representing a quasi-normal distribution type, with the primary pore radius of 20~60 μm. The pore volume of the small pores and large pores gradually decreased, showing approximately normal distribution characteristics (Figure 11a). In stepped distribution, the pore volume of <10 μm was basically stable within a certain range, and the pore volume of >10 μm was relatively large, with the relative value of around 10%~25% (Figure 11b). Regarding the unimodal characteristic, the primary pore volume was contributed by the pores of 10~20 μm in size, and the remaining pores contribute less to the volume (Figure 11c).

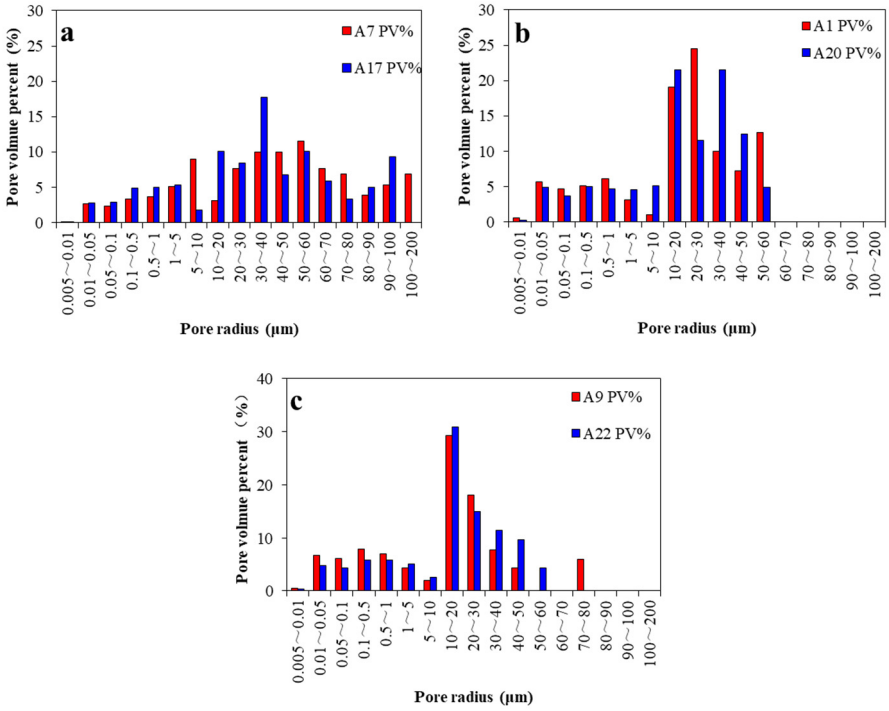

Figure 11. Full-scale pore radius analysis without CT scanning. (**a**) Representative samples with quasi-normal distribution characteristics; (**b**) representative samples with stepped distribution characteristics; (**c**) representative samples with unimodal distribution characteristics.

The physical properties of rocks control the type of histogram obtained, if the proportion of big pores is high, the physical properties are good. In general, if there are a large number of pores which are >60 μm, then the permeability is generally >5 mD. If there are many pore radii between 20 and 50 μm, the permeability is 0.5~2 mD. If there any many pore radii which are <20 μm, the permeability is generally <0.5 mD.

Unlike shale, the pores of sandstone are still dominated by nearly cylindrical shapes, with fewer highly irregular pores, so the physical properties of the rock are mainly controlled by the larger pores.

4. Results and Discussion of Quantitative Method

Quantitative experiments mainly include mercury intrusion and CT, and the recalculation of mercury intrusion data is shown in Section 3.4. CT can obtain quantitative pore data, but the experimental report is reconstructed using a ball-and-stick model. Data reprocessing requires the extraction of CT raw data, including pore volume and pore surface area data, which can be converted into a cylindrical model based on the introduced tortuosity index.

4.1. Results and Recalculation of CT

4.1.1. Result of the Ball-and-Stick Model

The visual characterization of the pore radius of the core mainly relies on CT scanning technology for analysis. The employment of a miniature core plug, with a diameter of 2 mm and a length of 2~3 mm, can improve the identification accuracy to 1~2 μm. CT scan data contains information such as pore radius, pore volume, pore frequency, throat radius, throat section, throat length, etc. [39,40]. In a broad sense, the throat also remains a pore [41–43]. The CT scan used digital reconstruction to describe the pore connectivity and pore space distribution with three-dimensional images, which can visually reflect the pore size distribution and connectivity.

After CT reconstruction (Figure 12), it can be seen that the pore radius of sample A1 was smaller (ball-and-stick model r < 50 μm), and the average coordinate was 1.14, i.e.,

on average, each pore was connected to 1.14 adjacent pores, reflecting poor connectivity and a permeability < 0.5 mD, correspondingly. The pores of Sample A7 contain a large number of medium-large pores (ball-and-stick model 50~200 μm), and there are many super-large pores (ball-and-stick model r > 200 μm), with an average coordinate of 3.22, reflecting good connectivity and a corresponding permeability > 5 mD. Sample A26 has a medium pore radius (ball-and-stick model 50~100 μm), and an average coordinate of 1.62, respectively. That is, each pore was connected to 1.62 adjacent pores, reflecting relatively poor connectivity and a permeability of <1 mD, correspondingly.

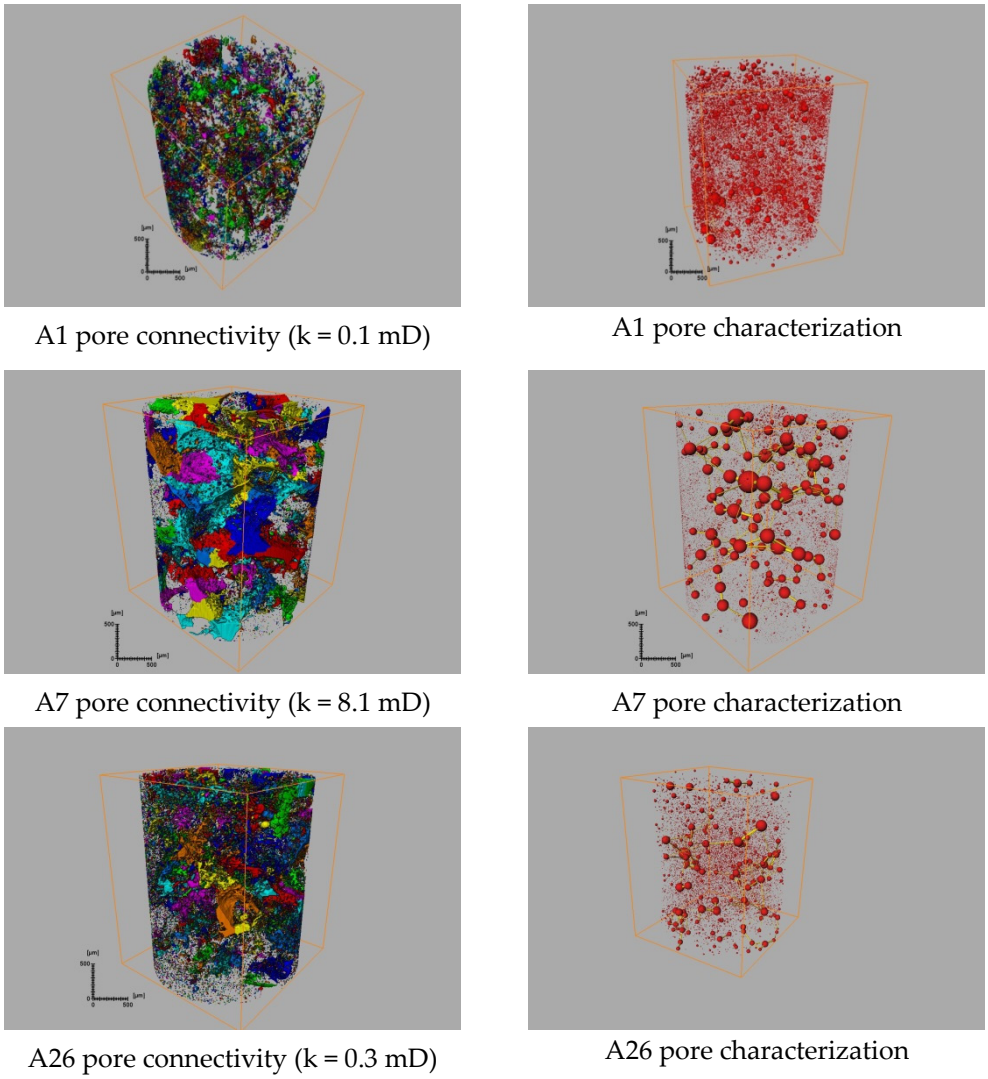

Figure 12. Three-dimensional reconstruction of the pore space of the core samples, with different permeability (ball-and-stick model).

4.1.2. Introduction of Cylinder Model

The primary experimental methods for pore size distribution, such as the transformation of NMR T_2 spectrum into the pore radius, use the cylinder model, and the high-pressure mercury intrusion calculation was conducted by using the cluster tube model to calculate the relationship between the mercury inlet pressure and the pore radius. The cylinder model was still used for analyzing the pore radius and the pore volume distribution of the cast thin sections; therefore, the paper introduced the cylinder model of the CT scan to recalculate the original CT data. The original CT data included pore volume, pore surface area, throat volume, and throat surface area. Under the same volume, the more complex the spatial distribution of the pores, the larger the surface area. Based on this, the tortuosity

τ was introduced, which was based on the ratio of the practical surface area of the pore and the equivalent spherical area:

$$\tau = \frac{S}{S_{eq}} = \frac{S \times r_{eq}}{3 \times V} = \frac{S}{3V} \times \sqrt[3]{\frac{3V}{4\pi}} = \frac{1}{\sqrt[3]{36\pi}} \times \frac{S}{\sqrt[3]{V^2}} \quad (8)$$

In this formula, τ is the tortuosity; S is the pore surface area data in the CT data; S_{eq} is the pore volume equivalent spherical surface area; r_{eq} is the equivalent spherical radius; V is the pore volume in the CT data.

By simplifying the pore space into a cylindrical model, two parameters were created, the radius r of the bottom surface and the height l, and taking $l = 2\tau r$, the equation can be obtained: $V = 2\tau\pi r^3$, namely,

$$r = \sqrt[3]{\frac{V}{2\tau\pi}} \quad (9)$$

Here, r is the equivalent cylinder radius; V is the volume parameter in the original CT data; τ is the tortuosity calculated by Formula (8). The pore radius r and the corresponding pore volume are counted in sections to obtain a histogram showing the pore radius distribution.

The pore distribution types of the CT cylindrical models for different samples are relatively similar (Figure 13). The frequency of the pore volume varies significantly when the pore radius is less than 20 μm, while the frequency is 0.1% when the A5 pore radius sample is less than 20 μm. The pore radius of the A10 and A45 samples is less than 20 μm, and the average frequency is about 0.8%. The frequency of a pore radius greater than 50 μm is generally around 10%, and the difference is the maximum pore radius. If the physical properties are good, the maximum pore radius can be up to 130 μm (Figure 13 A45), but if the physical properties are poor, the maximum pore radius gradually decreases (Figure 13 A5 A25 A10).

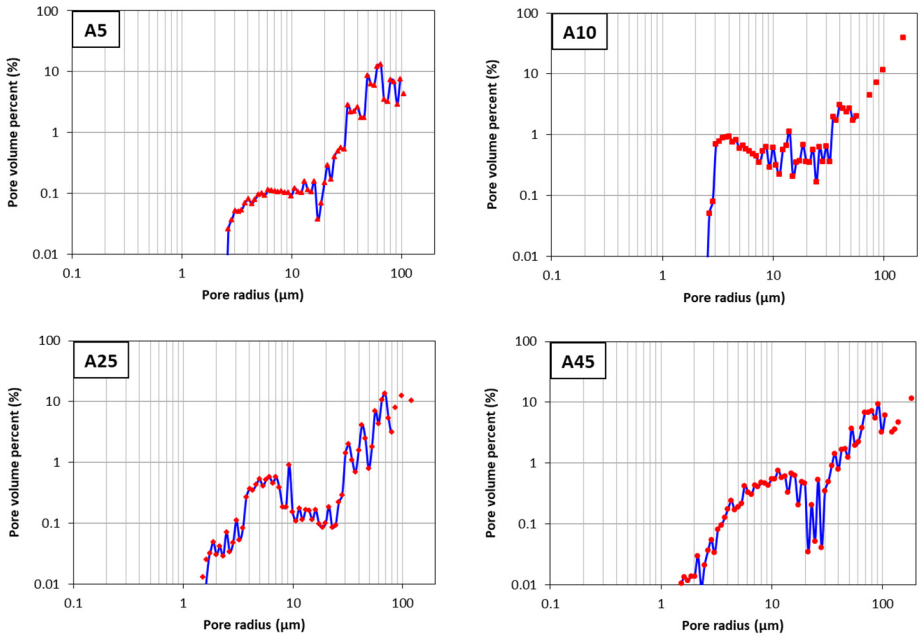

Figure 13. CT scan pore radius distribution curve based on a cylinder model.

4.2. Quantitative Method of Full-Scale Pore Radius Distribution

When the experimental data includes a CT scan, the major pore radius range of the CT scan is 2~200 μm, and the pore radius distribution of the high-pressure mercury intrusion mercury withdrawal curve is 0.007~5.3 μm. Using CT and high-pressure mercury intrusion data, the core can be analyzed to obtain the full-scale pore radius.

The pore radius is calculated from the CT scan pore volume data, according to the cylinder model (see Section 3.3 for details), and the pore radius is processed according to the proportional step length. The proportional magnification was 1.0719, which was the same as the proportional magnification of the NMR data and the mercury intrusion data. The pore volume in each step is accumulated and added to obtain the parameters of the pore radius and the pore volume. The minimum value of the pore radius in the CT scan was 2.56 μm, and the maximum value of the mercury withdrawal pore size distribution was 5.3 μm. The root mean square method was used to process the overlapping portion. By combining high-pressure mercury intrusion and CT scanning, the pore size distribution of the rock in the range of 7 nm~200 μm can be identified (Figure 14).

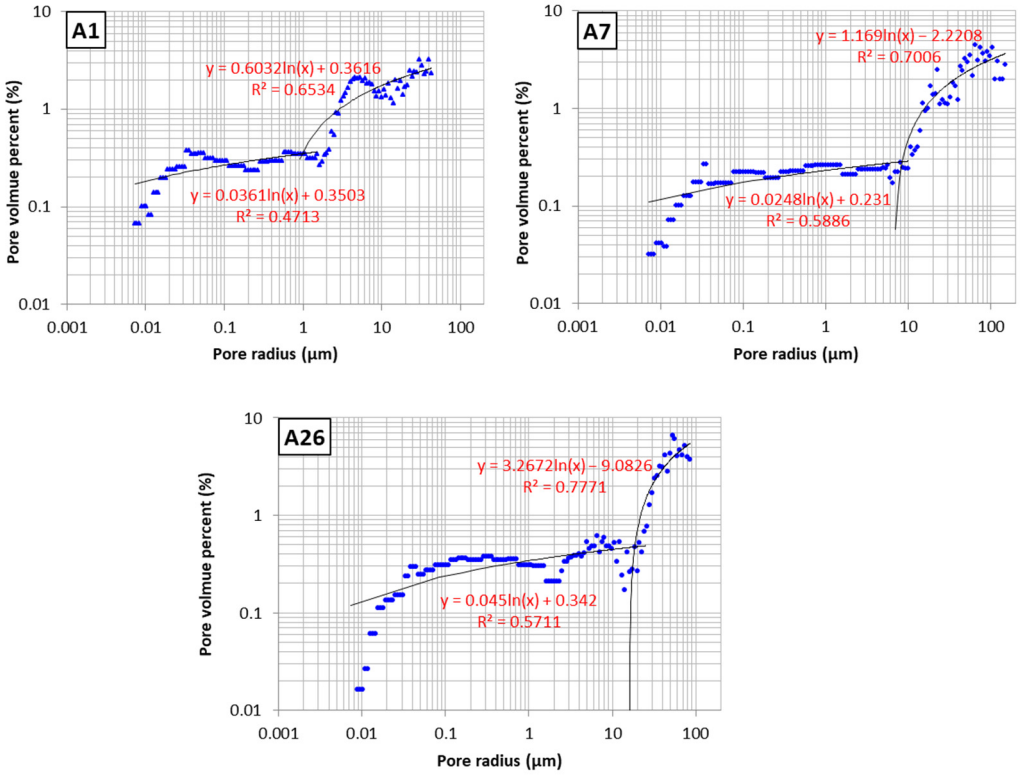

Figure 14. Full-scale pore radius analysis curve with CT scan–mercury intrusion data.

In this paper, there were three samples in which high-pressure mercury intrusion data and CT scan data were obtained simultaneously, namely A1 (Well A-1, 3449 m), A7 (Well A-2, 3614.9 m), and A26 (Well D-1, 5106.9 m), with porosity values of 7.6%, 10%, and 8.5% and permeability values of 0.1 mD, 8.1 mD, and 0.37 mD, respectively. The pore size distribution of the fine sandstone samples was basically a two-step type, and the step intervals and step heights of the samples with diverse porosity and permeability values were different. For Sample A1, the range of 0.007~2 μm was the first step, and the pore volume percentage was basically 0.3%. The step range of 2~40 μm was the second step, and the pore volume percentage was basically 2%~3% (Figure 14 A1). For Sample A7, the 0.007~10 μm was the first step, with a pore volume percentage of 0.2%~0.3%. The range of 10~150 μm was the second step, with a pore volume percentage of 1%~4% (Figure 14 A7). For Sample A26, the range of 0.007~20 μm was the first step, with the pore volume percentage of 0.3%~0.5%. The range of 20~90 μm was the second step, with the pore volume percentage of 3%~5% (Figure 14 A26).

The pore volume fitting line is logarithmic, and the pore volume and pore radius satisfy the function:

$$P_{v1} = a_1 \times \ln(r_1) + b_1 \quad (10)$$

for a small pore. Where P_{v1} is the small pore volume percent, %; r_1 is the small pore radius, μm; in this study area, a small pore is generally <10 μm; a_1 and b_1 are small pore function parameters.

$$P_{v2} = a_2 \times \ln(r_2) + b_2 \quad (11)$$

for a big pore. Where P_{v2} is the big pore volume percent, %; r_2 is the small pore radius, μm; in this study area, a big pore is generally >10 μm; a_2 and b_2 are big pore function parameters.

Full-scale pore radius distribution is controlled by five parameters: r_{max}, a_1, b_1, a_2, and b_2. The function parameter a_2 is proportional to the core porosity, and parameter b_2 is inversely proportional to the core porosity; however, its degree of fit is not high (Figure 15a,b). If the small pore parameters are stable, then a_1 is 0.025~0.045, and b_1 is 0.025~0.035 (Figure 14). The maximum pore radius is significantly related to core permeability (Figure 15c). If the empirical values are used for a_1 and b_1, then the parameters used to control the full-scale pore radius distribution curve can be determined.

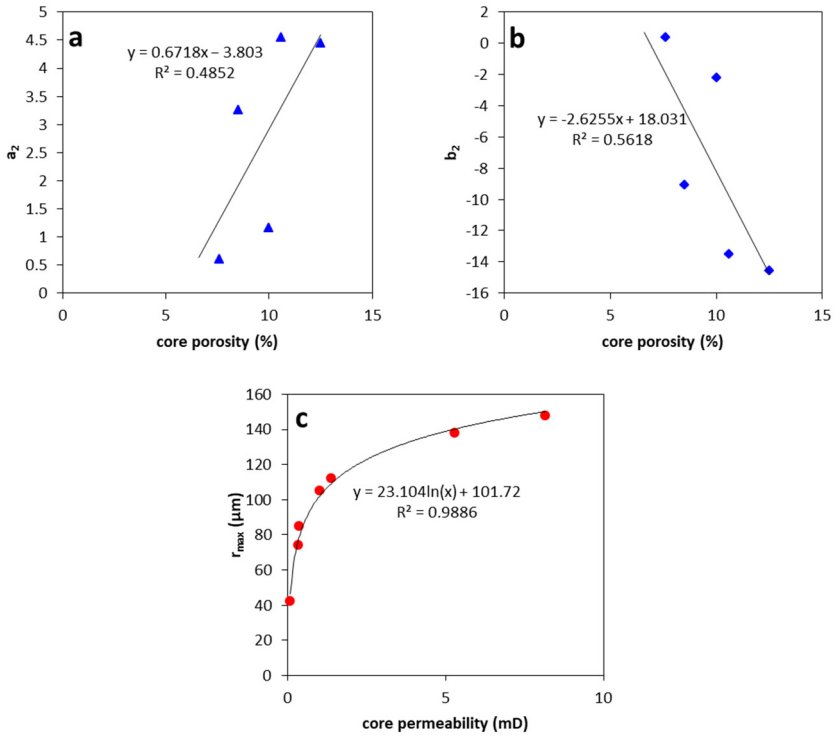

Figure 15. Relationship between function parameters and sandstone properties. (**a**) relationship between big pore coefficient and porosity; (**b**) relationship between big pore constant and porosity; (**c**) relationship between max radius and permeability.

The pore volume frequency is determined by the following formula:

$$P_v = \max[P_{v1}; P_{v2}] = \max\,[0.35\ln(r) + 0.3; (0.67p - 3.8)\ln(r) - 2.6p + 18] \quad (12)$$

The limiting conditions are:

$$r \in [0.007; 27\ln(k) + 101] \quad (13)$$

where r is the pore radius, μm; and K is the permeability; mD.

The logarithmic formula indicates that the physical properties of rocks are almost entirely influenced by large pores, and it can be considered that the pores of sandstone are relatively regular and closer to cylinders in shape. The contribution of large pores to physical properties is much greater than that of multiple small pores in the same volume.

Some scholars used nitrogen adsorption and high-pressure mercury injection data to study the full pore size characteristics of shale [44,45], and the obtained full pore size

data range is generally 0.002~10 μm. This study did not change the numerical model, but used the weighted average method to splice the two experiments, but failed to establish the formula of full pore size distribution.

The unified use of cylindrical numerical models in this article is more reliable. Another innovation of this article is the establishment of a quantitative mathematical relationship between rock properties and full-scale radius distribution.

5. Conclusions

This article mainly uses a unified numerical model to recalculate experimental data, using quantitative and semi-quantitative methods to study the distribution of pore structures. Due to the different types of experimental shale and sandstone, this method is mainly suitable for tight sandstone.

(1) In fine sandstone, the thickness of strongly bound water is about 0.04 μm, and the thickness of weakly bound water is about 0.35~0.4 μm, when the pore radius is less than 0.35~0.4 μm, and the relaxation time is completely controlled by surface relaxation.
(2) The surface relaxation rate ρ_2 of fine sandstone is generally about 18–20 μm/s.
(3) The quantitative logarithmic calculation of the full-scale radius distribution of sandstone has been established. The coefficient of the logarithm is positive with porosity, while the constant is negative with porosity. Permeability controls the maximum pore radius, with a max pore radius of >100 μm and a permeability of >1 mD.
(4) A semi-quantitative histogram showing the full pore size distribution of sandstone was completed. The histogram represents quasi-normal, stepped, and unimodal data. When 60 μm is the inflection point, a large proportion of pores measuring > 60 μm indicates good reservoir quality. If a large proportion of the pores measure < 60 μm, the permeability is generally <0.5 mD.

Author Contributions: Methodology, Z.H. and G.Y.; Data curation, J.C.; Writing—original draft, J.C.; Writing—review & editing, J.C., W.Z., Y.P. and T.Q.; Supervision, Z.H. All authors have read and agreed to the published version of the manuscript.

Funding: This research was funded by National Science and Technology Major Project (2016ZX05027-002-001).

Data Availability Statement: Raw data reserved.

Acknowledgments: The authors thank the State Key Laboratory of Oil and Gas and Resource Exploration, China University of Petroleum (Beijing), Suzhou Tainiu Testing Co., Ltd., and Huang for his guidance in writing the paper, as well as Zhang, Dong, and Li, who served as project team members and provided assistance in writing this paper.

Conflicts of Interest: The authors declare no conflict of interest.

References

1. Clarkson, C.R.; Freeman, M.; He, L.; Agamalian, M.; Melnichenko, Y.B.; Mastalerz, M.; Bustin, R.; Radliński, A.; Blach, T. Characterization of tight gas reservoir pore structure using USANS/SANS and gas adsorption analysis. *Fuel* **2012**, *95*, 371–385. [CrossRef]
2. Clarkson, C.R.; Solano, N.; Bustin, R.M.; Bustin, A.M.M.; Chalmers, G.R.L.; He, L.; Melnichenko, Y.B.; Radliński, A.P.; Blach, T.P. Pore structure charac-terization of north american shale gas reservoirs using usans/sans, gas adsorption, and mercury intrusion. *Fuel* **2013**, *103*, 606–616. [CrossRef]
3. Lai, J.; Wang, G.; Wang, Z.; Chen, J.; Pang, X.; Wang, S.; Zhou, Z.; He, Z.; Qin, Z.; Fan, X. A review on pore structure characterization in tight sandstones. *Earth-Sci. Rev.* **2018**, *177*, 436–457. [CrossRef]
4. Gao, H.; Cao, J.; Wang, C.; He, M.; Dou, L.; Huang, X.; Li, T. Comprehensive characterization of pore and throat system for tight sandstone reservoirs and associated permeability determination method using SEM, rate-controlled mercury and high pressure mercury. *J. Pet. Sci. Eng.* **2018**, *174*, 514–524. [CrossRef]
5. Gane, P.A.C.; Ridgway, C.J.; Lehtinen, E.; Valiullin, R.; Furó, I.; Schoelkopf, J.; Paulapuro, H.; Daicic, J. Comparison of NMR Cryoporometry, Mercury Intrusion Porosimetry, and DSC Thermoporosimetry in Characterizing Pore Size Distributions of Compressed Finely Ground Calcium Carbonate Structures. *Ind. Eng. Chem. Res.* **2004**, *43*, 7920–7927. [CrossRef]

6. Guo, X.; Huang, Z.; Zhao, L.; Han, W.; Ding, C.; Sun, X.; Yan, R.; Zhang, T.; Yang, X.; Wang, R. Pore structure and multi-fractal analysis of tight sandstone using MIP, NMR and NMRC methods: A case study from the Kuqa depression, China. *J. Pet. Sci. Eng.* **2019**, *178*, 544–558. [CrossRef]
7. Daigle, H.; Johnson, A. Combining Mercury Intrusion and Nuclear Magnetic Resonance Measurements Using Percolation Theory. *Transp. Porous Media* **2015**, *111*, 669–679. [CrossRef]
8. Sun, Y.; Zhai, C.; Xu, J.Z.; Cong, Y.Z.; Qin, L.; Zhao, C. Characterisation and evolution of the full size range of pores and fractures in rocks under freeze-thaw conditions using nuclear magnetic resonance and three-dimensional X-ray micros-copy. *Eng. Geol.* **2020**, *271*, 105616. [CrossRef]
9. Wei, Q.; Zhang, X.; Hu, J.; Zhu, B.; Lian, W.; Sun, W. Full-size pore structure characterization of deep-buried coals and its impact on methane adsorption capacity: A case study of the Shihezi Formation coals from the Panji Deep Area in Huainan Coalfield, Southern North China. *J. Pet. Sci. Eng.* **2019**, *173*, 975–989. [CrossRef]
10. Sasov, A.; Liu, X.; Salmon, P.L. Compensation of Mechanical Inaccuracies in Micro-CT and Nano-CT. In *Proceedings Volume 7078, Developments in X-ray Tomography VI*; SPIE: San Diego, CA, USA, 2008; Volume 7078. [CrossRef]
11. Bai, B.; Zhu, R.; Wu, S.; Yang, W.; Gelb, J.; Gu, A.; Zhang, X.; Su, L. Multi-scale method of Nano(Micro)-CT study on microscopic pore structure of tight sandstone of Yanchang Formation, Ordos Basin. *Pet. Explor. Dev.* **2013**, *40*, 354–358. [CrossRef]
12. Wardlaw, N.C.; McKellar, M. Mercury porosimetry and the interpretation of pore geometry in sedimentary rocks and artificial models. *Powder Technol.* **1981**, *29*, 127–143. [CrossRef]
13. Kaufmann, J.; Loser, R.; Leemann, A. Analysis of cement-bonded materials by multi-cycle mercury intrusion and ni-trogen sorption. *J. Colloid Interface Sci.* **2009**, *336*, 730–737. [CrossRef] [PubMed]
14. Nie, R.-S.; Zhou, J.; Chen, Z.; Liu, J.; Pan, Y. Pore structure characterization of tight sandstones via a novel integrated method: A case study of the Sulige gas field, Ordos Basin (Northern China). *J. Asian Earth Sci.* **2021**, *213*, 104739. [CrossRef]
15. Liu, Z.-N.; Wang, G.-T. A novel method for settlement calculation of semi-rigid pile composite foundation. *J. Hefei Univ. Technol. Nat. Sci.* **2006**, *6*, 1158–1160.
16. Kloubek, J. Investigation of Porous Structures Using Mercury Reintrusion and Retention. *J. Colloid Interface Sci.* **1994**, *163*, 10–18. [CrossRef]
17. Ouzzane, J.E.; Okuyiga, M.; Gomaa, N.; Ramamoorthy, R.; Rose, D.A.; Boyd, A.J.; Allen, D.F. Application of NMR T2 Relaxation to Drainage Capillary Pressure in Vuggy Carbonate Reservoirs. In Proceedings of the SPE Annual Technical Conference and Exhibition, San Antonio, TX, USA, 24–27 September 2006. [CrossRef]
18. Eslami, M.; Kadkhodaie, A.; Sharghi, Y.; Golsanami, N. Construction of synthetic capillary pressure curves from the joint use of NMR log data and conventional well logs. *J. Pet. Sci. Eng.* **2013**, *111*, 50–58. [CrossRef]
19. Sima, L.; Wang, C.; Wang, L.; Wu, F.; Ma, L.; Wang, Z. Effect of pore structure on the seepage characteristics of tight sandstone reservoirs: A case study of Upper Jurassic Penglaizhen Fm reservoirs in the western Sichuan Basin. *Nat. Gas Ind. B* **2017**, *4*, 17–24. [CrossRef]
20. Chen, S.; Tang, D.; Tao, S.; Ji, X.; Xu, H. Fractal analysis of the dynamic variation in pore-fracture systems under the action of stress using a low-field NMR relaxation method: An experimental study of coals from western Guizhou in China. *J. Pet. Sci. Eng.* **2019**, *173*, 617–629. [CrossRef]
21. Brookshire, D.S.; Chang, S.E.; Cochrane, H.; Olson, R.A.; Rose, A.; Steenson, J. Direct and indirect economic losses from earthquake damage. *Earthq Spectra* **1997**, *14*, 683–701. [CrossRef]
22. Fang, T.; Zhang, L.; Liu, N.; Zhang, L.; Wang, W.; Yu, L.; Li, C.; Lei, Y. Quantitative characterization of pore structure of the Carboniferous–Permian tight sandstone gas reservoirs in eastern Linqing depression by using NMR technique. *Pet. Res.* **2018**, *3*, 110–123. [CrossRef]
23. Dong, J.; Huang, Z.; Chen, J.; Zhang, W.; Wang, L.; Li, T.; Huang, Q.; Liu, L. A new method to establish NMR T2 spectrum based on bimodal Gaussian density function: A case study of tight sandstone in East China Sea Basin. *J. Pet. Sci. Eng.* **2018**, *167*, 628–637. [CrossRef]
24. Adey, B.; Hajdin, R.; Brudwile, E. Effect of common cause failures on indirect costs. *J. Bridge Eng.* **2004**, *9*, 200–208. [CrossRef]
25. Forcellini, D. A new methodology to assess indirect losses in bridges subjected to multiple hazards. *Innov. Infrastruct. Solut.* **2019**, *4*, 10. [CrossRef]
26. Glorioso, J.C.; Aguirre, O.; Piotti, G.; Mengual, J.-F. Deriving Capillary Pressure and Water Saturation from NMR Transversal Relaxation Times. In Proceedings of the SPE Latin American and Caribbean Petroleum Engineering Conference, Port-of-Spain, Trinidad and Tobago, 27–30 April 2003. [CrossRef]
27. Li, M.; Wang, D.; Shao, Z. Experimental study on changes of pore structure and mechanical properties of sandstone after high-temperature treatment using nuclear magnetic resonance. *Eng. Geol.* **2020**, *275*, 105739. [CrossRef]
28. Xiao, D.; Jiang, S.; Thul, D.; Huang, W.; Lu, Z.; Lu, S. Combining rate-controlled porosimetry and NMR to probe full-range pore throat structures and their evolution features in tight sands: A case study in the Songliao Basin, China. *Mar. Pet. Geol.* **2017**, *83*, 111–123. [CrossRef]
29. Karakouzian, M.; Farhangi, V.; Farani, M.R.; Joshaghani, A.; Zadehmohamad, M.; Ahmadzadeh, M. Mechanical Characteristics of Cement Paste in the Presence of Carbon Nanotubes and Silica Oxide Nanoparticles: An Experimental Study. *Materials* **2021**, *14*, 1347. [CrossRef]

30. Zhao, Y.; Yu, Q. CO_2 breakthrough pressure and permeability for unsaturated low-permeability sandstone of the Ordos Basin. *J. Hydrol.* **2017**, *550*, 331–342. [CrossRef]
31. Zhao, Y.; Zhang, Q.; Chen, X. Experimental investigation on effect of water film thickness in unsaturated sandstone cores on CO_2 transport during geologic storage. *J. Hydrol.* **2021**, *601*, 126595. [CrossRef]
32. Zdziennicka, A.; Jańczuk, B. Wettability of quartz by aqueous solution of cationic surfactants and short chain alcohols mixtures. *Mater. Chem. Phys.* **2010**, *124*, 569–574. [CrossRef]
33. Pan, B.; Li, Y.J.; Xie, L.J.; Wang, X.P.; He, Q.K.; Li, Y.C. Role of fluid density on quartz wettability. *J. Pet. Sci. Eng.* **2019**, *172*, 511–516. [CrossRef]
34. Chen, C.; Wan, J.; Li, W.; Song, Y. Water contact angles on quartz surfaces under supercritical CO_2 sequestration condi-tions: Experimental and molecular dynamics simulation studies. *Int. J. Greenh. Gas Control.* **2015**, *42*, 655. [CrossRef]
35. Shang, J.; Flury, M.; Harsh, J.B.; Zollars, R.L. Contact angles of aluminosilicate clays as affected by relative humidity and exchangeable cations. *Colloids Surf. A Physicochem. Eng. Asp.* **2010**, *353*, 1–9. [CrossRef]
36. Arogun, O.; Nwosu, C. Capillary Pressure Curves from Nuclear Magnetic Resonance Log Data in a Deepwater Turbidite Nigeria Field—A Comparison to Saturation Models from SCAL Drainage Capillary Pressure Curves. In Proceedings of the Nigeria Annual International Conference and Exhibition, Abuja, Nigeria, 30 July–3 August 2011. [CrossRef]
37. Chatzis, I.; Dullien, F. Mercury porosimetry curves of sandstones. Mechanisms of mercury penetration and withdrawal. *Powder Technol.* **1981**, *29*, 117–125. [CrossRef]
38. Niu, Q.; Revil, A. Connecting complex conductivity spectra to mercury porosimetry of sedimentary rocks. *Geophysics* **2016**, *81*, E17–E32. [CrossRef]
39. Desbois, G.; Urai, J.L.; Kukla, P.A.; Konstanty, J.; Baerle, C. High-resolution 3D fabric and porosity model in a tight gas sandstone reservoir: A new approach to investigate microstructures from mm- to nm-scale combining argon beam cross-sectioning and SEM imaging. *J. Pet. Sci. Eng.* **2011**, *78*, 243–257. [CrossRef]
40. Golab, A.N.; Knackstedt, M.A.; Averdunk, H.; Senden, T.; Butcher, A.; Jaime, P. 3D porosity and mineralogy characterization in tight gas sandstones. *Lead. Edge* **2010**, *29*, 1476–1483. [CrossRef]
41. Qu, Y.; Sun, W.; Tao, R.; Luo, B.; Ren, D. Pore–throat structure and fractal characteristics of tight sandstones in yanchang formation, ordos basin. *Mar. Pet. Geol.* **2020**, *120*, 104573. [CrossRef]
42. Shao, X.; Pang, X.; Jiang, F.; Li, L.; Huyan, Y.; Zheng, D. Reservoir Characterization of Tight Sandstones Using Nuclear Magnetic Resonance and Incremental Pressure Mercury Injection Experiments: Implication for Tight Sand Gas Reservoir Quality. *Energy Fuels* **2017**, *31*, 10420–10431. [CrossRef]
43. Zhu, H.H.; Zhang, T.S.; Zhong, D.K.; Li, Y.Y.; Zhang, J.C.; Chen, X.H. Binary pore structure characteristics of tight sand-stone reservoirs. *Pet. Explor. Dev.* **2019**, *46*, 226–235. [CrossRef]
44. Xiao, D.; Lu, Z.; Jiang, S.; Lu, S. Comparison and integration of experimental methods to characterize the full-range pore features of tight gas sandstone—A case study in Songliao Basin of China. *J. Nat. Gas Sci. Eng.* **2016**, *34*, 1412–1421. [CrossRef]
45. Zhang, L.; Lu, S.; Xiao, D.; Gu, M. Characterization of full pore size distribution and its significance to macroscopic physical parameters in tight glutenites. *J. Nat. Gas Sci. Eng.* **2016**, *38*, 434–449. [CrossRef]